Article

Journal of the Brazilian Chemical Society

https://dx.doi.org/10.21577/0103-5053.20240101

J. Braz. Chem. Soc. **2024**, *35*, 11, e-20240101, 1-14

Electrocatalysis of Oxygen Evolution Reaction by Iron Oxide Nanomaterials Synthesized with *Camellia sinensis* Extract

Samara L. Machado,[a] Ana Luisa Silva,[a] Ana Paula N. de Souza,[a] Dalber R. Sánchez,[b] Mariella Alzamora,[c] Jefferson S. de Gois[a] and Nakédia M. F. Carvalho*[,a]

[a]*Instituto de Química, Universidade do Estado do Rio de Janeiro, Rua São Francisco Xavier, 524, Maracanã, 20550-013 Rio de Janeiro-RJ, Brazil*

[b]*Instituto de Física, Universidade Federal Fluminense, Av. Gal. Milton Tavares de Souza s/nº, Gragoatá, 24210-346 Niterói-RJ, Brazil*

[c]*Universidade Federal do Rio de Janeiro, Campus Duque de Caxias, Rodovia Washington Luiz, 19593, Santa Cruz da Serra, 25240-005 Duque de Caxias-RJ, Brazil*

The generation of clean, zero-carbon, and renewable energy is a challenge for the development of a sustainable and egalitarian society. Hydrogen gas can be produced by water electrolysis and has been claimed as the most promising option to replace fossil fuels. The oxygen evolution reaction (OER) is the most energetically demanding step of the water splitting and requires the use of electrocatalysts to overcome the kinetic barrier. Iron oxide nanomaterials have been emerging as a low-cost and Earth-abundant OER electrocatalysts. The synthesis of iron oxide assisted by plant extract is an eco-friendly approach to obtain nanomaterials with unique properties. Herein, we investigated iron oxide synthesized with the assistance of *Camellia sinensis* extract, under different experimental conditions towards oxygen evolution reaction electrocatalysis. Pure phases of iron oxide were obtained, ferrihydrite and maghemite showed overpotentials of 460 and 480 mV at a current density of 10 mA cm^{-2}, respectively. After calcination, hematite was formed and the overpotential was raised to 610 and 810 mV, respectively. The lower overpotential of the amorphous materials could be related to the lower electron transfer resistance and faster reaction rate. On the other hand, the calcinated materials presented higher specific activity, stability and higher Faradaic efficiency.

Keywords: oxygen evolution reaction, electrocatalysis, iron oxide, plant extract, renewable energy, black tea

Introduction

The energetic crisis combined with environmental deterioration and climate changes, demand urgent substitution of the fossil fuels by renewable and carbon-free sources of energy. The harnessing of solar energy to accomplish the water electrolysis to produce green hydrogen fuel has been sought as one of the best alternatives for the energy transition. However, many challenges must be overcome to diminish the energetic cost of the water splitting in hydrogen and oxygen (equation 1), especially the thermodynamic barrier and sluggish kinetics of the anodic oxygen evolution reaction (OER, equation 2).

$$2H_2O \rightarrow O_2 + 2H_2 \qquad E^0 = -1.23\ V \qquad (1)$$

$$O_2 + 4e^- + 4H^+ \rightarrow 2H_2O \qquad E^0 = +1.23\ V \qquad (2)$$

$$2H^+ + 2e^- \rightarrow H_2 \qquad E^0 = 0\ V \qquad (3)$$

Electrocatalysts are necessary to overcome the kinetic barrier of the OER and diminish the inherent overpotential. Materials based on noble metal elements such as Ru and Ir are among the most active electrocatalysts, but the high cost, low stability and scarcity pose obstacles to the implementation of commercial electrolyzers.[1] Therefore, Earth-abundant elements as the first-row transition metals are the best choice for the production of scalable and cost-effective electrocatalyst for the anode of the overall water splitting process.[2,3]

*e-mail: nakedia@uerj.br
Editor handled this article: Célia M. Ronconi (Associate)
The first time I heard about the incredible world of nanoscience was from Prof Oswaldo in one of his many courses and lectures that I attended during my undergraduate degree in Chemistry.

Iron is one of the most Earth-abundant elements. Recently, iron oxide nanomaterials have been emerging as OER electrocatalysts with promising applications due to unique properties such as magnetism, low toxicity, rich redox chemistry and reactive towards oxygen-species. Strategies such as doping, creation of oxygen vacancies and defects have been described to diminish the poor electrical conductivity and increase its OER activity. Structural properties such as coordination environment, crystalline phase and orientation, and surface facets have an importance in the OER catalytic performance.[4]

Green synthesis of metal oxides assisted by plant extracts has been described as a low-cost, non-toxic, and eco-friendly alternative to the energy-demanding, high-cost, and generation of hazardous wastes of the chemical and physical methods. Natural polyphenolic compounds act as reducing and capping agents in the formation of green iron oxide nanoparticles under mild conditions.[5] Recently, green oxides of the transition metal elements Fe,[5] Ni,[6] Cu,[7-9] Cu/Co,[10] have been used as simple and versatile electrocatalysts for OER and water splitting applications.[1]

Green iron oxide nanomaterials synthesized with the assistance of plant extract have been poorly explored in the OER electrocatalysis and represent a promising alternative to provide nanomaterials with unique properties. Fe_3O_4 nanoparticles (NPs) of average size around 5 nm and a high surface area of ca. 150 m^2 g^{-1} were synthesized using the aqueous extract of *Pandanus odoratissimus* leaves and were tested in the electrocatalysis of OER at pH 13. The overpotential at 1 mA cm^{-2} was 320 mV (ca. 750 mV at 10 mA cm^{-2}).[5] Beyond this single report on green iron oxides prepared with plant extract for OER electrocatalysis, iron coordination network prepared with the polyphenol tannic acid was applied in the OER electrocatalysis exhibiting an overpotential of 324 mV at 10 mA cm^{-2} and pH 14.[11] When iron-tannic acid was supported on carbon nanotubes or conductive carbon fiber paper, the reported overpotentials at 10 mA cm^{-2} and pH 14 were 420[12] and 410 mV,[13] respectively.

The hydrogen production through water splitting greatly depends on the development of efficient, cost-effective, and sustainable OER electrocatalysts. To address this point, we explored magnetic iron oxide nanomaterials synthesized with the assistance of *Camellia sinensis* extract, in the OER electrocatalysis. *Camellia sinensis* is a well-known polyphenol-rich plant that has been extensively applied in the synthesis of metal and metal oxide nanomaterials. *Camellia sinensis* as black tea has been previously applied in the synthesis of green iron oxides for environmental remediation applications,[14-17] but has not been applied to OER electrocatalysis. Herein, we explored different experimental conditions in the synthesis of the iron oxide, such as the order of the addition of the reagents and the calcination. The materials were characterized by X-ray diffraction (XRD), Fourier transform infrared spectroscopy (FTIR) and Mössbauer spectroscopy, thermogravimetric analysis (TGA), derivative thermal analysis (DTG), scanning electron microscopy (SEM) and X-ray energy-dispersive spectrometer (SEM-EDS). The OER essays were carried out under alkaline conditions by linear sweep voltammetry (LSV), and the electrochemical characterization of the materials was carried out by electrochemical impedance spectroscopy (EIS).

Experimental

Materials

All chemicals were of reagent grade and were used without further purification. *Camellia sinensis* as black tea from Dr. Oetker (São Paulo, Brazil) brand, composed of leaves and stems, was purchased from a local market. $FeCl_2{\cdot}4H_2O$, $FeCl_3{\cdot}6H_2O$, isopropyl alcohol (≥ 99.8%), the Folin-Ciocalteu phenol reagent (2.0 mol L^{-1}) and 5% Nafion 117 aqueous solution were purchased from Sigma-Aldrich (St. Louis, MO, United States), KOH (≥ 85.0%) was purchased from Merck (New Jersey, USA), NH_4OH was purchased from Caledon (Ontario, Canada). All aqueous solutions were prepared with deionized water. Fluoride tin oxide (FTO) glass plates with 13 Ω *per* square surface resistivity were purchased from Sigma-Aldrich (St. Louis, MO, United States). FTO glass plates were previously cut into slides of 1 cm × 3.5 cm, and before deposition, the FTO slides were first sonicated in soap water, then in ethanol and acetone for 10 min, and finally rinsed with deionized water before use.

Camellia sinensis extract preparation and characterization

The extract was prepared with 3.6 g of black tea in 60 mL of deionized water (60 g L^{-1}) under heating at 80-90 °C and magnetic stirring for 60 min, followed by filtration of the tea residue.

The total polyphenol content (TPC) of the extract was determined by the Folin-Ciocalteu method following the published procedure[18] and TPC was expressed in milligrams of gallic acid equivalents *per* gram of leave (mg EGA g^{-1}). Qualitative tests were performed to determine the presence of the following phytochemicals in the black tea extract: phenols, alkaloids, coumarins, tannins, quinones, terpenoids, and flavonoids; as described in detail in the Supplementary Information (SI) section.[19] High-performance liquid chromatography

coupled with a diode array detector (HPLC-DAD) analyses were performed in an Agilent 1260 Infinity instrument (Agilent Technologies, Santa Clara, CA, USA) equipped with a ChemStation software, a G1311B 1260 Quat Pump, a G1321B 1260 FLD, an autosampler, and a reverse-phase column Pursuit 5 C18 column from Agilent (250 mm length × 4.6 mm internal diameter, 5 μm particle size). The DAD detector was set at 280, 320, and 360 nm, and the peak area was monitored. The analyses were performed in gradient elution, with solvent A (95% of acetic acid in ultrapure water) and solvent B (20% of solvent A and 80% of CH_3CN). The flow rate was 1.0 mL min^{-1} with an injection volume of 20 μL, a column temperature of 25 °C, a working pressure of 130 MPa, and a running time of 47 min. The extract was characterized by cyclic voltammetry by dilution of 3 mL in 25 mL of phosphate buffer (pH 6.7),[20] using a potentiostat/galvanostat Autolab PGSTAT302N, Metrohm (Herisau, Switzerland). A three-electrode system was used as an electrolytic cell, using a freshly polished 3.0 mm glassy carbon as working electrode (Metrohm), Pt rod as counter-electrode (Metrohm), and Ag|AgCl (3.0 mol L^{-1} KCl) as reference electrode, from 0 to 1 V at 100 mV s^{-1}.

Iron oxide synthesis

The iron oxide nanomaterial was synthesized by slow addition of the black tea extract (60 mL) to a mixture of $FeCl_3 \cdot 6H_2O$ (0.10 mol L^{-1}) and $FeCl_2 \cdot 4H_2O$ (0.05 mol L^{-1}) in 24 mL of H_2O, at room temperature and under stirring. Both solutions were degasified with Ar before the mixture. Once the tea extract was added, the iron salt solution changed its color from yellow to dark brown, indicating the formation of iron oxide. Then, 2.1 mL of NH_4OH were added to the mixture, and the black precipitate formed was named Fe_2O_3-A. After 1 h of reaction, the solid was filtered, washed with water and ethanol, and dried in a rotary evaporator at 60 °C.

The same procedure was set up, but the NH_4OH solution was first added to the $Fe^{II/III}$ solution under stirring, and after that, the black tea extract (60 mL) was added. The solution immediately changed the color to black even before the tea extract was added, due to the formation of iron oxides with the base. The black precipitate formed was named Fe_2O_3-B.

A portion of each sample was calcined at 600 °C for 4 h using a muffle furnace, resulting in two new samples named Fe_2O_3-AC and Fe_2O_3-BC.

Characterization methods

X-ray diffraction patterns were obtained using an X 'Pert PRO diffractometer (Philips, Panalytical, Almelo, The Netherlands) equipped with monochromatic Cu Kα radiation (λ = 1.540 Å). The measurements were taken within a 2θ angle range of 20 to 80°, step size of 0.0131° and a scan rate of 0.04° min^{-1}. FTIR was carried out using a PerkinElmer Frontier Single & Dual Range (Waltham, MA, United States) spectrophotometer with KBr pellets. Thermogravimetric analyses were carried out using a Netzsch (Selb, Germany) thermogravimetric system (STA 449 F1 Jupiter). The sample, weighing 10 mg, was placed in an alumina crucible and heated from 35 to 900 °C at a rate of 10 °C min^{-1}. The heating was carried out under a synthetic air flow of 45 mL min^{-1}. Mössbauer spectroscopy of ^{57}Fe experiments were performed at room temperature and 4.3 K in transmission geometry with the Co-57 Rh-matrix source moving in a sinusoidal mode (WissEl, Starnberg, Germany). The low-temperature experiments were performed in a JANIS cryostat. The powdered samples were cooled down inside the cryostat while the source was kept at room temperature outside of the cryostat. The hyperfine parameter isomer shift (IS) values are expressed related to metallic iron. SEM analysis was performed in a Jeol 7100FT (Akishima, Japan) (LaMAR/CAIPE-UFF) equipped with an EDS 80 mm^2 single-shot detector (SDD), Oxford Instruments (Abingdon, United Kingdom).

Working electrode preparation

Films of the iron oxide nanomaterials were prepared in Pt rotating disk electrode (RDE from Metrohm) with a diameter of 3 mm and area of 0.0707 cm^2 or in FTO glass plates of 1 cm^2.The modified working electrodes (WE) were used in EIS and OER experiments.

A suspension of 8.0 mg of the catalyst in 400 μL of deionized water, 98 μL of 2-propanol, and 10 μL of Nafion was sonicated for 10 min forming an ink with a dosage of 15.8 mg mL^{-1}. Then, 4 μL of the ink was pipetted onto the Pt RDE electrode and dried in an oven at 40 °C for 10 min, resulting in a catalyst loading of 0.89 mg cm^{-2}. Alternatively, 20 μL of the ink was pipetted onto the FTO electrode and dried in an oven at 40 °C for 10 min. The resulting catalyst loading was 0.31 mg cm^{-2}.

Electrochemical measurements

All the electrochemical characterization was conducted in an Autolab potentiostat/galvanostat PGSTAT302N (Metrohm, Herisau, Switzerland) controlled by NOVA software 2.1.5. A typical electrolytic cell of 30 mL was used, consisting of a three-electrodes system with

Ag|AgCl (3.0 mol L^{-1} KCl) as reference electrode, a counter-electrode of Pt bar (Metrohm), and a FTO glass plate modified with the oxide suspensions was used as working electrode. The electrochemical performance was investigated by EIS, at an applied potential of 1.5 V *vs*. reversible hydrogen electrode (RHE) in the frequency range of 1×10^{-5} to 1×10^{5} Hz. The electrochemically active surface area (ECSA) of the samples was calculated from the electrochemical double layer capacitance (C_{dl}) of the electrode, via cyclic voltammetry scan, conducted in a non-Faradaic region at different scan rates of 10 to 150 mV s^{-1} (equation 4), where the specific capacitance, C_s = 0.04 mF cm^{-2} and the electrode area, S = 1 cm^2.[21] Experimental data for ECSA (cm^2) calculation are shown in Table S6 (SI section).

$$ECSA = \frac{C_{dl}}{C_s / S} \quad (4)$$

Potentials were converted to the RHE scale by the relation (equation 5),

$$E_{RHE} = E_{Ag|AgCl} + 0.210V + 0.059V \times pH \quad (5)$$

where E_{RHE} is the potential in RHE scale, $E_{Ag|AgCl}$ is the potential in Ag|AgCl scale.

OER electrocatalytic tests

OER performance was accessed by LSV from 0.5 to 2.0 V *vs*. RHE, at a scan rate of 25 mV s^{-1} and room temperature in 1 mol L^{-1} KOH electrolyte at pH 14. A typical electrolytic cell of 30 mL was used, consisting of a three-electrodes system with Ag|AgCl (3.0 mol L^{-1} KCl) as reference electrode, a counter-electrode of Pt bar (Metrohm), and a Pt RDE modified with the catalysts films as working electrode at 1600 rpm. Stability tests were carried out by chronopotentiometry at 10 or 100 mA cm^{-2} in FTO working electrode.

The overpotential (η) for the OER was calculated according to equation 6.

$$\eta = E_{RHE} - 1.23V \quad (6)$$

OER Tafel slope was calculated by equation 7:

$$b = \frac{\partial \eta}{\partial \log\log(i)} = \frac{2.303RT}{\alpha F} \quad (7)$$

where b is the Tafel slope in mV dec^{-1}, η is the overpotential in V, R is the universal gas constant, T is the temperature in Kelvin, F is the Faraday constant and α is the coefficient of anodic transfer.

The turnover frequency (TOF) was calculated based on the catalyst loading m = 0.89 mg cm^{-2}, and the measured current density j (A cm^{-2}) at η = 0.40 V by equation 8:

$$TOF = \frac{jA}{4nF} \quad (8)$$

where A is the geometric area of the Pt disc is 0.0707 cm^2, n is the mol number of the coated catalyst, and F is the Faraday constant (96485 C mol^{-1}).

The mass activity values (A g^{-1}) are determined by dividing the measured current density j (mA cm^{-2}) at η = 0.40 V by the catalyst loaded at the electrode, m = 62.9 μg for RDE. This calculation can be expressed by equation 9:

$$\text{Mass activity} = \frac{j}{m} \quad (9)$$

The specific activity values (j_s / mA cm^{-1}) were determined by dividing the current i (mA) at η = 0.40 V by the ECSA. This calculation is expressed by equation 10:[21]

$$j_s = \frac{i}{ECSA} \quad (10)$$

Faradaic efficiency (η_F) was calculated using equation 11, where the volume of evolved oxygen was measured by volumetry and the calculated theoretical volume was calculated from the Faraday equation.[22]

$$\eta_F = \frac{V_{O_2\ measured}}{V_{O_2\ calculated}} \quad (11)$$

Results and Discussion

Characterization of the *Camellia sinensis* extract

The extract of black tea presented a TPC of 44.91 mg EGA g^{-1}, representing a high quantity of polyphenolic compounds, as described in the literature.[16] The qualitative tests indicated the presence of the main classes of polyphenols as tannins, phenols, and flavonoids (Table S1, SI section). By the HPLC-DAD analyses (Figures S1-S3, SI section) it was possible to detect gallic acid, protocatechuic acid, vanillic acid, syringic acid, *trans*-cinnamic acid, caffeic acid, coumaric acid, rutin (flavonoid) and quercetin (Figure 1a). It was also possible to observe a broad peak characteristic of tannins of higher molecular weight, such as tannic acid. Gallic

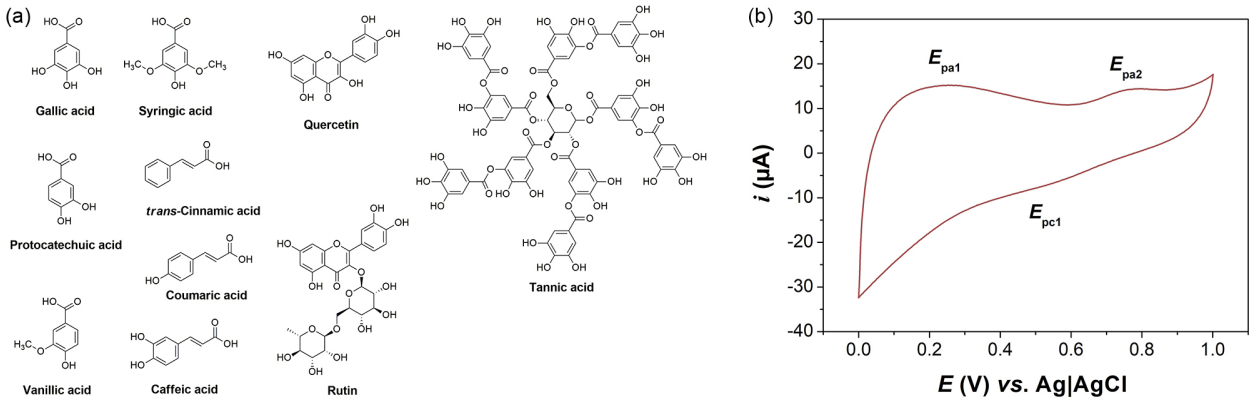

Figure 1. *Camellia sinensis* extract characterization. (a) Main polyphenolic compounds detected by HPLC-DAD; (b) cyclic voltammogram in phosphate buffer at 100 mVs^{-1}.

acid was the major polyphenol with a concentration of 5.85 mg g^{-1}, accounting for 13% of the TPC result. These compounds are well known for their capacity to chelate to metal ions, contributing to the nanoparticles formation and stabilization. The cyclic voltammetry of the black tea extract was acquired to study the electrochemical properties, as shown in Figure 1b. Two irreversible anodic peaks were observed at +0.26 and +0.79 V *vs*. Ag|AgCl, and one irreversible cathodic peak was observed around 0.50 V *vs*. Ag|AgCl. The E_{pa1} is characteristic of gallic acid, as described in the literature the anodic peak appears at +0.236 V *vs*. Ag|AgCl.[20] The E_{pa2} could be attributed to vanillic (+0.764 V *vs*. Ag|AgCl) or coumaric acid (+0.804 V *vs*. Ag|AgCl).[23] The main properties of the *Camellia sinensis* extract are shown in Table 1.

Table 1. Characterization data of the black tea extract

Property	*Camellia sinensis* extract
TPC[a] / (mg EGA g^{-1})	44.91
E_{pa1}[b] / V	+0.26 *vs*. Ag|AgCl
E_{pa2}[b] / V	+0.79 *vs*. Ag|AgCl
E_{pc1}[b] / V	+0.50 *vs*. Ag|AgCl
Phenolic compounds	tannins, phenols, and flavonoids;[c] gallic acid, protocatechuic acid, vanillic acid, syringic acid, *trans*-cinnamic acid, caffeic acid, coumaric acid, rutin (flavonoid) and isoquercetin[d]

[a]TPC: total polyphenol content (Folin-Ciocalteu); [b]cyclic voltammetry: E_{pa}: anodic peak potential; E_{pc}: cathodic peak potential; [c]qualitative tests; [d]HPLC-DAD: high-performance liquid chromatography coupled with a diode array detector.

Characterization of the iron oxide nanomaterials

The magnetic iron oxide nanomaterials were synthesized from $Fe^{II/III}$ ions and NH_4OH, with the assistance of *Camellia sinensis* extract. The polyphenols present in the black tea extract stabilize and protect the iron nanoparticles. The NH_4OH helps the formation and precipitation of the Fe_xO_y oxide, and two approaches were adopted: adding NH_4OH before or after the addition of the black tea extract, giving the samples named Fe_2O_3-B and Fe_2O_3-A, respectively. Both materials were calcined at 600 °C and resulted in two new samples: Fe_2O_3-BC and Fe_2O_3-AC. The synthesis procedure is summarized in Scheme 1 and the properties of the catalysts are summarized in Table 2.

The X-ray diffractograms of the iron nanomaterials are shown in Figure 2a. In general, broad diffraction peaks typical of amorphous material were observed, especially for the samples without calcination. In the case of the sample Fe_2O_3-B, distinct peaks associated with γ-Fe_2O_3 (maghemite, JCPDS card No. 39-1346) appeared. Upon calcination at 600 ºC, the sample Fe_2O_3-BC suffered a phase change to α-Fe_2O_3 (hematite, ICSD No. 201096). For the sample Fe_2O_3-A, the predominant amorphous profile did not allow the observation of well-defined peaks, precluding correlation with the characteristic iron oxide phase, however, upon calcination at 600 ºC, the obtained sample Fe_2O_3-AC presented the characteristic peaks of α-Fe_2O_3. The results indicated that the heat treatment removed the polyphenolic compounds and provided the formation of hematite, rendering them a more crystalline nature.[24,25] The crystalline structures of ferrihydrite, maghemite, and hematite are shown in Figure 3.

SEM images (Figures S4-S7, SI section) revealed the formation of amorphous and agglomerated particles, with irregular shapes and sizes ranging from 2 to 10 μm, observed for both pristine and calcined samples. After calcination at 600 °C, the XRD pattern showed narrower peaks for the calcined samples that may be associated with more crystalline phases, however, this does not lead to the formation of better-defined particles as observed in the SEM images, contrary to the findings of previous works.[16] SEM-EDS analysis (Figures S8-S9, SI section)

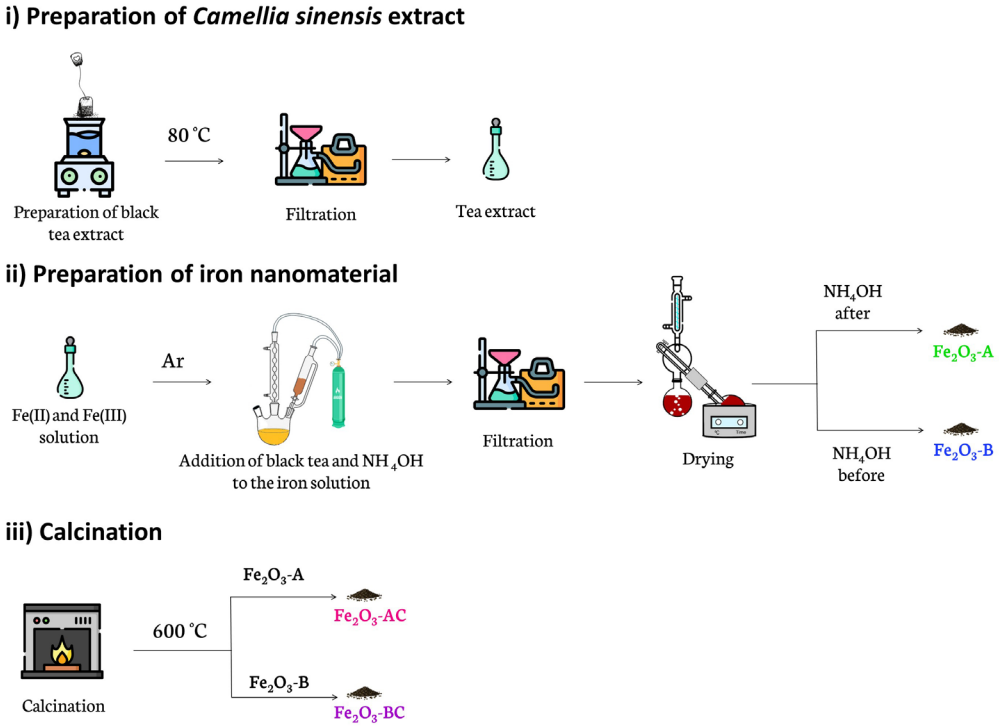

Scheme 1. Green synthesis of the iron oxide nanomaterials.

Table 2. Characterization data of the green iron oxide nanomaterials

Property	Fe_2O_3-A	Fe_2O_3-AC	Fe_2O_3-B	Fe_2O_3-BC
Main iron phase[a]	$Fe_5O_8H{\cdot}4H_2O$ ferrihydrite	α-Fe_2O_3 hematite	γ-Fe_2O_3 maghemite	α-Fe_2O_3 hematite
Main iron phase[a] / wt.%	96.4	100	100	100
Crystallite size[b] / nm	–	14.8	9.9	25.4
Fe[c] / wt.%	30.4	69.9	48.9	69.9
Organic[d] / wt.%	47.3	–	30.3	–
Residue[d] / wt.%	52.4	100	69.9	100

[a]Determined by Mössbauer spectroscopy; [b]calculated by Scherer equation from XRD (X-ray diffraction) data. For Fe_2O_3-A no well-defined XRD peak was observed; [c]determined by the residue of the thermogravimetric analysis (TGA) data and considering the wt.% of the iron phase from Mössbauer spectroscopy; [d]determined by TGA analysis.

of the samples showed C, Fe, and O as the main elements. The sample Fe_2O_3-A showed higher C and O content and lower Fe than Fe_2O_3-B, which is consistent with a higher organic content incorporated in the material when the NH_4OH is added after the mixture of $Fe^{II/III}$ and the black extract, leading to the formation of iron(II/III)-polyphenol complexes before precipitation with NH_4OH. After calcination, C decreased, and Fe and O were the major elements, confirming the removal of phenolic compounds from the black tea (Table S3, SI section).

The ^{57}Fe Mössbauer spectroscopy experiments were performed to provide information about the formation of the different phases along the chemical process. Figure 4a shows the room temperature and 4.3 K spectra of the Fe_2O_3-A sample. The spectrum at room temperature is properly fitted with two paramagnetic doublets whose hyperfine parameters are shown in Table 3. The doublet with isomer shift IS = 0.38 mm s^{-1} and quadrupolar splitting ΔE_Q = 0.78 mm s^{-1} is attributed to a Fe^{III} center. The doublet with IS = 1.08 mm s^{-1} and quadrupolar splitting ΔE_Q = 2.63 mm s^{-1} is attributed to Fe^{II} in polyphenol complex.[16,17] The 4.2 K spectrum reveals five sub spectra, two doublets corresponding to Fe^{II} and Fe^{III} corresponding to that observed at room temperature, and three sextets whose hyperfine parameters (Table 3) are compatible with the $Fe_5O_8H{\cdot}4H_2O$ ferrihydrite.[26,27] The small doublet corresponding to the Fe^{III} observed at 4.2 K could be related to very small ferrihydrite nanoparticles[26,28] that do not block

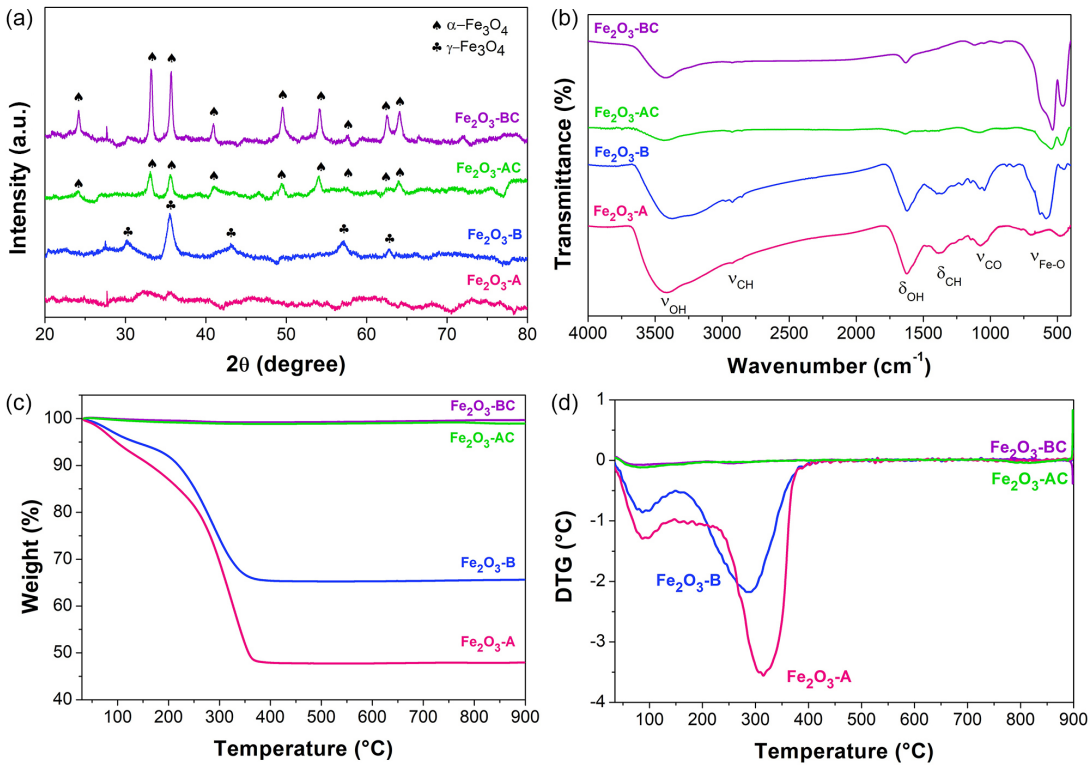

Figure 2. (a) X-ray diffraction patterns; (b) FTIR (KBr) spectra; (c) TGA curves; (d) DTG curves, for the green iron oxide nanomaterials.

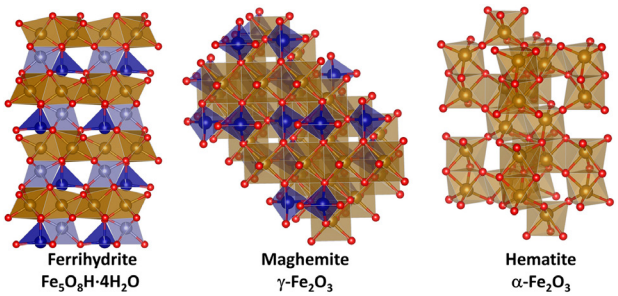

Figure 3. Crystalline structure of the phases observed in the green iron oxide nanomaterials.

even at low temperatures such as 4.2 K. So, the Mössbauer experiment shows that Fe_2O_3-A sample is formed by a polyphenol complex containing Fe^{II} and ferrihydrite.

Figure 4b displays the room temperature and 4.3 K Mössbauer spectra of the sample Fe_2O_3-B. The room temperature spectrum exhibits a small doublet corresponding to Fe^{III} and a broadened sextet properly fitted with a distribution of hyperfine magnetic fields with an average and most probable hyperfine field of 34.09 T (Table 3) and 44.90 T (Figure 4b), respectively. The hyperfine magnetic field distribution indicates the presence of a size distribution of nanoparticles. Here, it was also necessary to carry out measurements at low temperatures to correctly identify the corresponding phases. The Mössbauer spectrum at 4.2 K exhibits three well-resolved sextets whose hyperfine parameters correspond to maghemite.[26] These results indicate that all the nanoparticles of γ-Fe_2O_3 are blocked at 4.3 K. Therefore, these experiments showed that the sample is formed solely by maghemite, in agreement with the results of the X-ray experiments.

Figure 5 shows the room temperature Mössbauer spectra of the Fe_2O_3-AC and Fe_2O_3-BC samples after calcination at 600 ºC. Both spectra are nearly identically composed of three sextets whose hyperfine parameters are almost the same with only small differences in the ratios of the areas (Table 4). The hyperfine magnetic field (ca. 51.2 T) corresponds to the outermost lines of hematite.[26] The sextets with slightly smaller fields are attributed to smaller hematite nanoparticles.[29] Thus, the Mössbauer experiments confirm the presence of hematite in both calcined samples as had already been pointed out by XRD data.

The FTIR spectra of the samples (Figure 2b) before calcination show the characteristic bands of the phenolic compounds present in the black tea extract.[17] Both samples Fe_2O_3-A and Fe_2O_3-B presented, at approximately 3400 and 1600 cm^{-1}, bands related to the stretching vibration and angular deformation of OH groups of water, respectively.[30] Small bands at 2920 and 2854 cm^{-1} are characteristic of C–H bonds from aliphatic carbon. The absorption band at 1370 cm^{-1} corresponds to the angular vibration of the C–H bond of aromatic and aliphatic groups, and the vibrations at 1260 and 1070 cm^{-1} correspond to C–O groups while

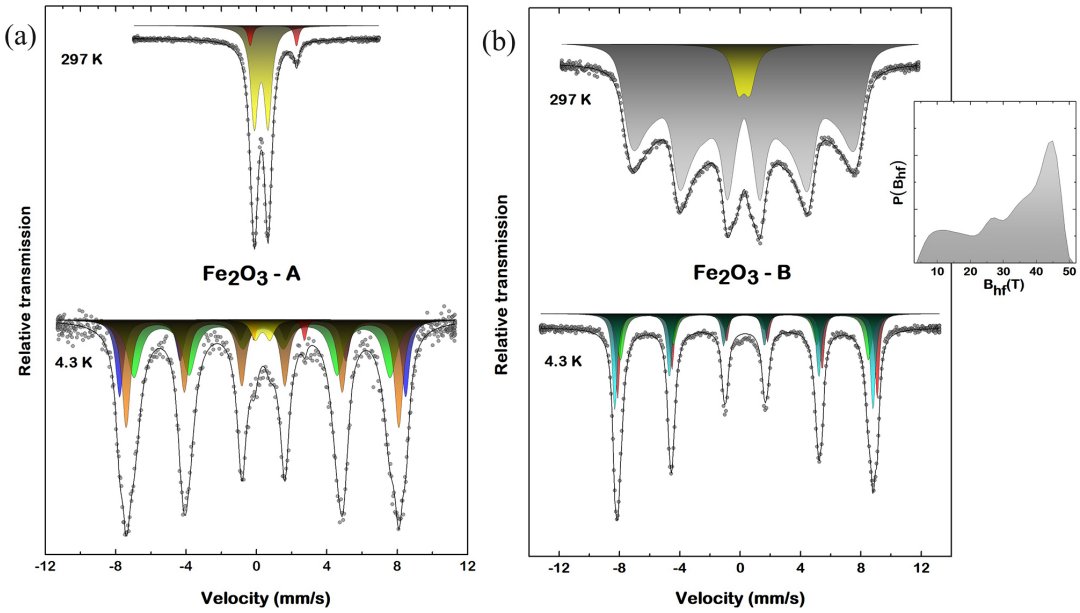

Figure 4. Room temperature (297 K) and 4.3 K Mössbauer spectra. (a) Fe_2O_3-A: the analysis of the spectra shows the presence of Fe^{II} in a tea complex (paramagnetic doublet) and ferrihydrite (sextets) as the majority phase. (b) Fe_2O_3-B: the analysis of the spectra shows the presence of maghemite nanoparticles. The broadened sextet at room temperature indicates a size distribution of nanoparticles.

Table 3. Mössbauer hyperfine parameter isomer shift (IS), quadrupolar splitting (ΔE_Q), linewidth (Γ), magnetic hyperfine field (B_{hf}), and absorption area (A) of the Fe_2O_3-A and Fe_2O_3-B samples taken from the fitting of the spectra recorded at room temperature and 4.3 K. The values in brackets correspond to the average values of the distribution magnetic hyperfine field fitting. The attribution for each site is indicated in the last column

Sample	Temperature / K	Site	IS / (mm s^{-1})	ΔE_Q / (mm s^{-1})	Γ / (mm s^{-1})	B_{hf} / T	Area / %	Attribution
Fe_2O_3-A	297	D1	0.38	0.78	0.50	–	93.0	Fe^{III}
		D2	1.08	2.63	0.30	–	7.0	Fe^{II}
	4.3	D1	0.46	0.83	0.60	–	2.8	Fe^{III}
		D2	1.41	2.87	0.30	–	0.8	Fe^{II}
		S3	0.47	–0.061	0.92	45.11	47.4	ferrihydrite
		S4	0.49	–0.040	0.58	48.04	32.6	ferrihydrite
		S5	0.48	–0.023	0.54	50.41	16.4	ferrihydrite
Fe_2O_3-B	297	D1	0.37	0.75	0.93	–	6.1	Fe^{III}
		S2	<0.36>	0.00	0.70	<34.09>	93.9	maghemite
	4.3	S1	0.59	0.025	0.34	53.36	24.7	maghemite
		S2	0.38	–0.010	0.39	53.10	35.6	
		S3	0.42	–0.030	0.59	50.99	39.7	

the two bands at 700 and 400 cm^{-1} are characteristic of Fe–O bonds of iron oxide.[16] In the calcined samples, the bands referring to the OH group and the Fe–O bond are predominant and the absence of the polyphenol bands confirmed the removal after calcination.

The quantity of organic compounds present in the nanomaterials was measured by TGA and DTG analysis as can be seen in Figures 2c-2d. The TGA-DTG curves of the Fe_2O_3-A and Fe_2O_3-B samples revealed two main regions of weight loss. Region I (30-160 °C) corresponds to the release of water and region II (160-400 °C) corresponds to the loss of organic compounds, with the maximum weight loss occurring around 300 ºC. Sample Fe_2O_3-A presents 47.3 wt.% of organic compounds, while Fe_2O_3-B presents 30.3 wt.%. After reaching 900 ºC, 52.4 wt.% of residue for Fe_2O_3-A and 69.9 wt.% for Fe_2O_3-B remained. This difference is coherent with a higher organic content incorporated in the material when the NH_4OH is added after the mixture of $Fe^{II/III}$ and the black tea extract, leading to the formation of iron(II/III)-polyphenol complexes before precipitation with NH_4OH. For the Fe_2O_3-BC and Fe_2O_3-AC samples, only one region was revealed, in which there was only 0.3 and 1% mass loss, respectively, indicating that all the organic material was removed

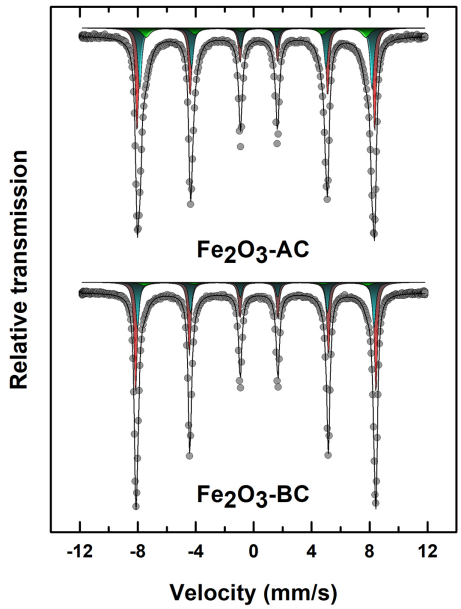

Figure 5. Room temperature Mössbauer spectra of the Fe_2O_3-AC and Fe_2O_3-BC samples calcinated at 600 ºC. The hyperfine parameters of the sextets (Table 4) correspond to hematite.

with the previous heat treatment at 600 °C carried out on the samples. Tables S4-S5 (SI section) summarize the TGA data.

Scheme 2 shows the proposed mechanism for the synthesis of the green iron oxide assisted by *Camellia sinensis* extracts rich in polyphenolic compounds, majorly gallic acid as determined by HPLC. When NH_4OH is added after the mixture of the iron salt and black tea (Fe_2O_3-A), the first step corresponds to the bound of the OH phenolic groups to the Fe^{II}/Fe^{III} ions. In the second step, the NH_4OH is added and induces the formation of iron oxide nanoparticles of ferrihydrite, probably through Ostwald ripening or coalescence. The resulting amorphous nanoparticles contain the organic compounds incorporated in the bulk of the oxide. When NH_4OH is added before the mixture of the iron salt and black tea (Fe_2O_3-B), first the iron oxide nanoparticles of maghemite are formed. In the second step, the black tea extract is added and the nanoparticles are capped/stabilized by the tea polyphenols. In the third step, the annealing step removes the polyphenols and forms the crystalline phase of hematite.[16]

OER electrocatalysis

To assess the electrocatalytic OER activity of the prepared iron oxides, linear sweep voltammetry was performed for RDE Pt films at a scan rate of 25 mV s^{-1},

Table 4. Mössbauer hyperfine parameter of the Fe_2O_3-AC and Fe_2O_3-BC samples calcinated at 600 ºC. Isomer shift (IS), quadrupolar splitting (ΔE_Q), linewidth (Γ), magnetic hyperfine field (B_{hf}) and absorption area (A) taken from the fitting of the spectra recorded at room temperature. The attribution for each site is indicated in the last column

Sample	Site	IS / (mm s^{-1})	ΔE_Q / (mm s^{-1})	Γ / (mm s^{-1})	B_{hf} / T	Area / %	Attribution
	S1	0.37	–0.18	0.70	47.08	24.4	hematite
Fe_2O_3-AC	S2	0.38	–0.20	0.32	49.69	33.7	hematite
	S3	0.38	–0.21	0.27	50.88	41.9	hematite
	S1	0.38	–0.19	0.72	47.76	13.6	hematite
Fe_2O_3-BC	S2	0.38	–0.22	0.28	50.59	28.9	hematite
	S3	0.38	–0.22	0.26	51.44	57.5	hematite

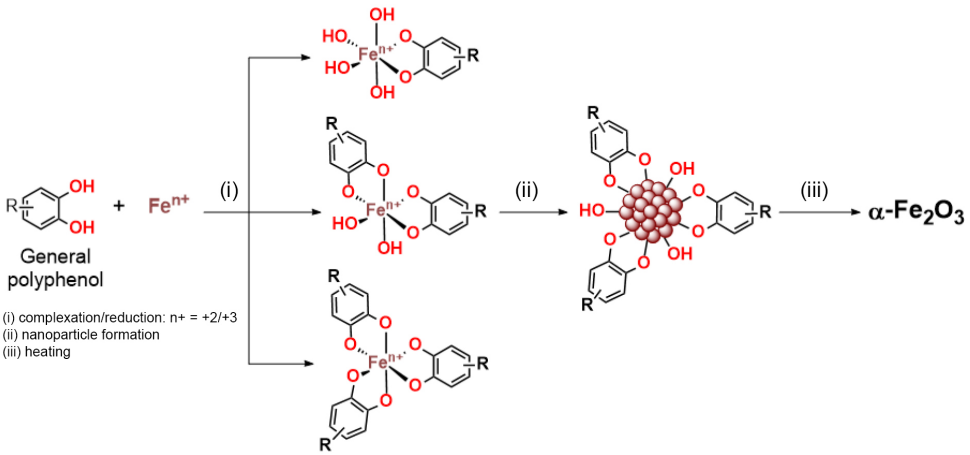

Scheme 2. Green iron oxide nanomaterial synthesized with the assistance of *Camellia sinensis* extract.

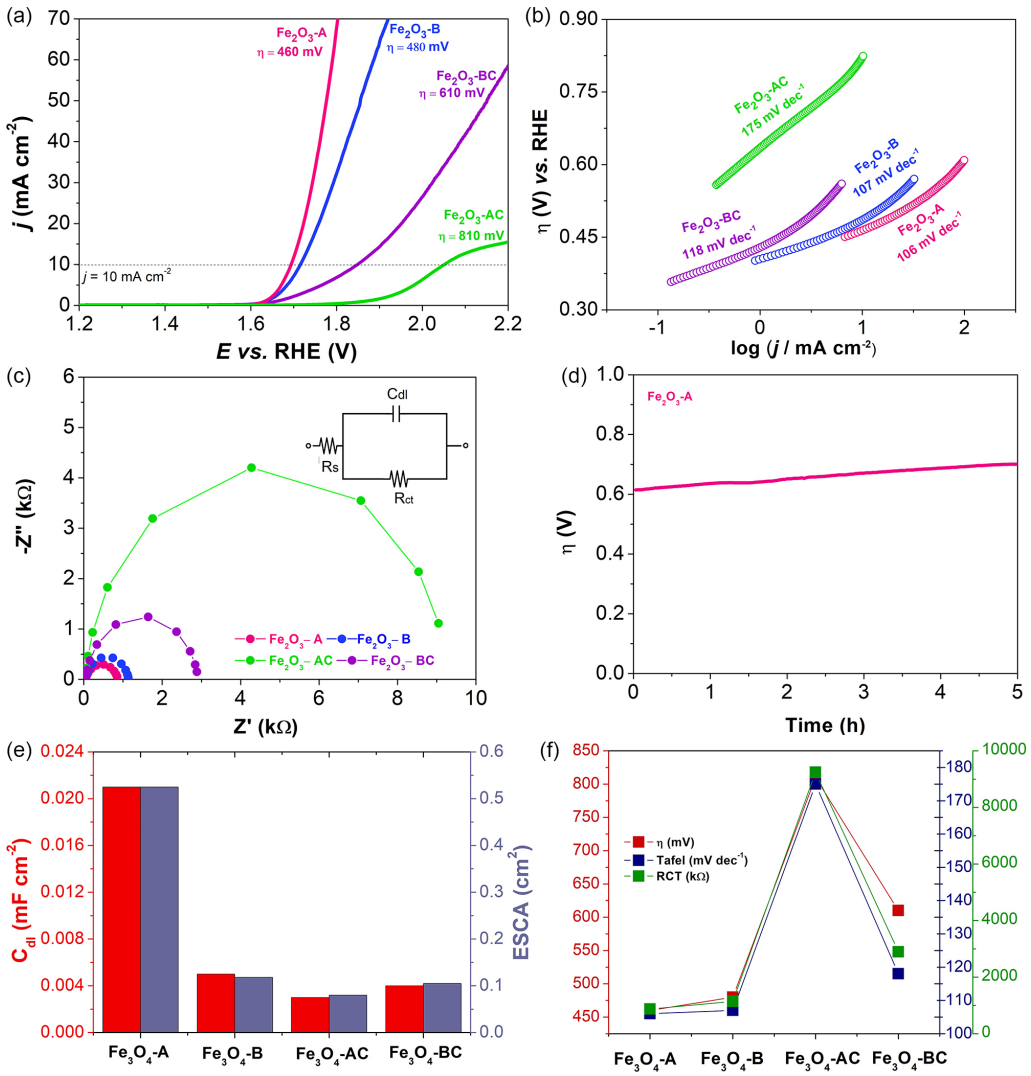

Figure 6. Electrochemical characterization of films of the catalysts: (a) polarization LSV curves for OER in Pt RDE electrode and (b) respective Tafel plots in 1 mol L^{-1} KOH solution, at a scan rate of 0.025 Vs^{-1}. (c) Nyquist plots of the electrochemical impedance spectra and (d) C_{dl} and ECSA, (e) chronopotentiometric curve with a constant current density of 10 mA cm^{-2}; (f) comparative graph of the relationship with overpotential, Tafel slopes and R_{ct} for OER activity.

Table 5. Electrochemical data for the OER at pH 14 catalyzed by the synthesized iron oxides

Catalyst	Main phase	η_{10} / mV	$j_{s,400}$ / (mA cm^{-2})	TOF_{400} / s^{-1}	TOF_{400}/Fe / s^{-1}	TOF_{400}/ECSA / (s^{-1} cm^{-2})	Tafel / (mV dec^{-1})	ECSA / cm^2	R_{ct} / Ω	η_F / %
Fe_2O_3-A	$Fe_5OH_8{\cdot}4H_2O$	460	0.12	4.27×10^{-4}	1.41×10^{-3}	7.77×10^{-4}	106	0.550	870	53
Fe_2O_3-B	γ-Fe_2O_3	480	0.52	3.87×10^{-4}	5.53×10^{-4}	3.42×10^{-3}	107	0.113	1144	99
Fe_2O_3-AC	α-Fe_2O_3	810	0.056	3.21×10^{-5}	6.56×10^{-5}	3.69×10^{-4}	175	0.087	9246	98
Fe_2O_3-BC	α-Fe_2O_3	610	0.35	2.25×10^{-4}	3.21×10^{-4}	2.29×10^{-3}	118	0.098	2895	88

Main phase determined by XRD and Mössbauer spectroscopy; overpotential at $j = 10$ mA cm^{-2}: η_{10}; specific activity at $\eta = 400$ mV: $j_{s,400}$; turnover frequency at $\eta = 400$ mV: TOF_{400}; Tafel slope; ECSA: electrochemically active surface area; R_{ct}: charge transfer resistance; η_F: Faradaic efficiency. Complete data is shown in Table S6 (SI section). TOF/Fe = TOF/[(Fe wt.% estimated from residue in TGA curve)/100)] (TGA: thermogravimetric analysis)

1 mol L^{-1} KOH solution at pH 14, as presented in Figure 6a. The metrics used to compare the catalytic activity of the different catalysts are shown in Table 5.

The overpotential defined at j = 10 mA cm^{-2} was measured based on the geometric area of the working electrode. Among the green iron nanomaterials prepared, Fe_2O_3-A exhibited the lowest overpotential at η_{10} of 460 mV followed by Fe_2O_3-B, Fe_2O_3-BC, and Fe_2O_3-AC with 480, 610, and 810 mV, respectively. The TOF values were calculated at $\eta = 400$ mV presenting the same trend as the

overpotential, Fe_2O_3-A with 4.27×10^{-4} s^{-1} showing the highest value among the catalysts. When TOF is divided by the weight percentage of iron oxide in the material determined by the TGA data, the TOF is even higher for Fe_2O_3-A, 8.90×10^{-4} s^{-1}. Dividing the TOF by the iron percentage, more noticeable catalytic activity was revealed, with TOF of 1.41×10^{-3} s^{-1} for Fe_2O_3-A. These results indicated that the as-prepared nanomaterials provide more oxygen evolution at a lower overpotential than the calcined samples, probably because they present more defects and oxygen vacancies than the crystalline analogues. It was shown that amorphous mixed-metal oxides containing iron were more active than the comparable crystalline materials and provided OER performance comparable to noble metal oxides.[31] Furthermore, Fe_2O_3-A and Fe_2O_3-B present the hydrous ferric oxyhydroxide ferrihydrite and maghemite phases, while the calcinated oxides present the hematite phase. Ferrihydrite synthesized by a chemical route was described as active for OER electrocatalysis, an overpotential of around 420 mV was observed at 10 mA cm^{-2} and pH 14.[32] Maghemite is also an active catalyst for OER and showed an overpotential of 390 mV at pH 14.[33] However, hematite has been associated with lower OER electrocatalytic activity with 510 mV, especially when compared to amorphous iron oxides.[31,33]

Comparison of Fe_2O_3-A with the literature shows comparable or higher activity to reported iron oxide nanomaterials (Table S7, SI section). Fe_3O_4 NPs synthesized using the aqueous extract of *Pandanus odoratissimus* leaves and reached an overpotential of ca. 750 mV at 10 mA cm^{-2}, much higher than Fe_2O_3-A with η_{10} of 460 mV.[5] Iron-tannic acid exhibited an overpotential of 324 mV at 10 mA cm^{-2} and pH 14,[11] when supported on carbon nanotubes or on conductive carbon fiber paper, the reported overpotentials at 10 mA cm^{-2} at pH 14 were 420[12] and 410 mV,[13] respectively. Amorphous FeOx prepared by a chemical synthesis from $Fe(CO)_5$ shows an overpotential of 427 mV at ca. 10 mA cm^{-2}, which presented lower overpotential than the crystalline Fe_3O_4 with 534 mV.[4]

The kinetic parameter describing the OER electron transfer reaction at the electrode interface was examined to evaluate the catalyst performance, utilizing the Tafel slope depicted in Figure 6b. A lower Tafel slope indicates an improvement in OER kinetics due to enhanced electron transfer capacity and strongly coupled effects. Lower Tafel slopes were obtained for Fe_2O_3-A followed by Fe_2O_3-B, Fe_2O_3-BC, and Fe_2O_3-AC with 106, 107, 118, and 175 mV dec^{-1}, respectively. Ferrihydrite prepared by chemical route presented 104 mV dec^{-1}, a very close value of Fe_2O_3-A.[32]

EIS measurements showed a lower resistance to charge transfer (R_{ct}) for the as-prepared catalysts (Figure 6c). The material Fe_2O_3-AC presented considerably higher R_{ct}, which can explain the higher overpotential obtained amongst the materials (Figure 6f). This result corroborated with the low activity of hematite in relation to ferrihydrite and maghemite. This behavior can also be associated with the sintering of the nanoparticles during calcination. The higher OER activity of the catalysts without the thermal treatment is corroborated by the higher values for double layer capacitance and electrochemically active surface area (Figure 6e). In particular, Fe_2O_3-A presented C_{dl} and ECSA around 7 times higher than Fe_2O_3-AC, and around 5 times higher than Fe_2O_3-B, indicating that the higher ECSA contributes to the higher activity presented by Fe_2O_3-A.

The specific activity at the overpotential of 400 mV was calculated to compare the intrinsic activity of catalysts with different ECSA. The ideal catalyst will have a low overpotential, be stable over time, and have a high specific activity.[21] The normalized OER current at 400 mV (equation 10) by the ECSA, followed the order: Fe_2O_3-B > Fe_2O_3-BC > Fe_2O_3-A > Fe_2O_3-AC (Tables 5 and S6). Catalyst Fe_2O_3-B presented a higher specific activity than Fe_2O_3-A because it presented a lower ECSA. The TOF/ECSA followed the same order. The higher ECSA and consequently the higher roughness factor would indicate porous materials that could difficult the mass-transport of OH^- to the interior active sites within the pores and make them catalytically inaccessible during OER.[34] In order words, Fe_2O_3-A evolutes more oxygen because of the higher ECSA, however, the catalytic sites of Fe_2O_3-B are more active for OER. This difference could be attributed to the higher activity of the major phase of Fe_2O_3-B, γ-Fe_2O_3, in comparison with ferrihydrite that composed Fe_2O_3-A, as described in the literature (Table S7, SI section).

In addition, long-term stability is another important parameter used to evaluate electrocatalysts. Herein, the electrochemical stability of the Fe_2O_3-A film was examined in 1 mol L^{-1} KOH solution. As observed in Figure 6d, an overpotential of about 614 mV was needed to deliver a 10 mA cm^{-2} current density. After 5 h, a small increase in the overpotential to 700 mV was observed, implying the limited stability of the Fe_2O_3-A in 1 mol L^{-1} KOH solution, as confirmed by the leaching of the film of the catalyst during the experiment.

The Faradaic efficiency of the catalysts was investigated by chronoamperometry at higher current density of 100 mA cm^{-2} for 2 h. The volume of the oxygen evolved over time was measured by volumetry (Figures 7a-7b). All the materials present an increase in the overpotential in the first 30 min, the calcinated materials operated at lower potential than the respective as-prepared samples.

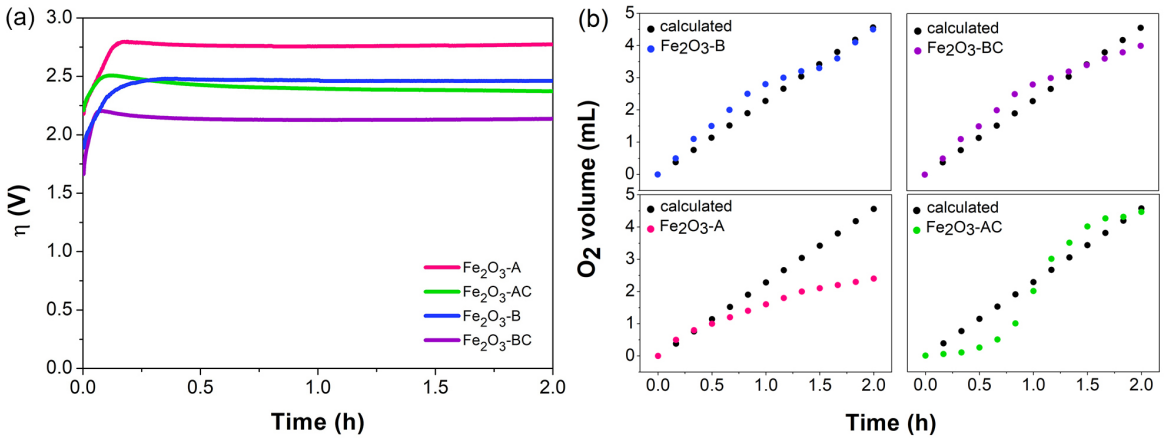

Figure 7. (a) Chronopotentiometric curves with a constant current density of 100 mA cm^{-2} at 1 mol L^{-1} KOH at FTO. (b) Corresponding Faradaic efficiency of the iron oxide nanomaterials.

Among then, Fe_2O_3-BC presented the lower overpotential at 100 mA cm^{-2}. The Faradaic efficiency (Table 5) stayed above 88%, the catalyst Fe_2O_3-B and Fe_2O_3-AC presented 99 and 98% of η_F, respectively. The catalyst Fe_2O_3-A presented the lower η_F, 53%, and the lower stability is also evidenced by the leaching of the film during the experiment. It was evident that the as-prepared samples are less stable and the film suffered leaching during the electrocatalysis, while the calcinated films resisted the 2 h of the test. Comparing the variation in the order of NH_4OH addition in the synthesis, the material Fe_2O_3-B, where NH_4OH was added before the black tea extract, was more stable and this may be attributed to the formation of maghemite protected by the polyphenols, but in the case of Fe_2O_3-A the polyphenols are trapped inside the bulk of the nano oxide and make the structure more susceptible to degradation under the high potential and pH of the OER conditions.

The FTO film of the catalysts Fe_2O_3-A and Fe_2O_3-AC were characterized by XRD before and after the OER electrocatalysis (Figure 8). From the diffractograms of Fe_2O_3-A and Fe_2O_3-AC it was not possible to observe any peak besides those of the FTO due to the amorphous nature of the oxide. After OER, new peaks appeared, which could be assigned to ferrihydrite and hematite phases formed by electrochemical activation. SEM images of Fe_2O_3-A (Figures S11-S12, SI section) showed a change in morphology after OER electrocatalysis, from an irregular spheroidal to an oriented branch-like morphology mainly composed of carbon, oxygen, and minor amounts of iron. Some particles of irregular spheroidal morphology like the fresh catalyst were also observed. In comparison with the fresh catalyst, the iron content estimated by the SEM-EDS analysis (Figures S11-S12, SI section) had decreased considerably, indicating leaching of the iron to the electrolyte. The SEM images of Fe_2O_3-AC showed a film covering the FTO surface and some spheroidal particles, majorly composed of carbon, oxygen, and iron, but in this case, the iron content was maintained after OER, indicating more stability of the calcinated material upon the electrocatalytic conditions.

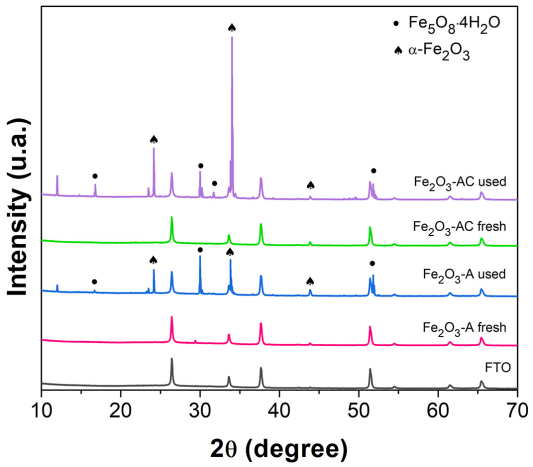

Figure 8. X-ray diffraction patterns for the green iron oxide nanomaterials deposited on FTO, before and after OER electrocatalysis.

Conclusions

Green iron oxide nanomaterials were synthesized with the assistance of *Camellia sinensis* extract, under different conditions of reaction, and were applied successfully as electrocatalysts in the oxygen evolution reaction under pH 14. Iron phases with high purity were obtained for all materials, according to the reaction condition. Ferrihydrite was obtained as the main phase of the material synthesized with NH_4OH added after the formation of Fe^{III}-polyphenol complexes, which was also the most amorphous, with higher organic content, and the nanomaterial with the lowest overpotential of 469 mV at current density of 10 mA cm^{-2}. Maghemite was the main phase obtained when NH_4OH was added to the iron salts before the plant extract, which

presented high OER activity with 480 mV of overpotential. After calcination at 600 °C, the amorphous nanomaterials were transformed into a more crystalline magnetite phase and the OER activity dropped significantly due to slower kinetics and higher electron transfer resistance, pointing out the lower overpotential of the amorphous materials in comparison with the crystalline ones. The higher ECSA also contributed to the higher TOF shown by the as-prepared materials. However, the calcinated materials were also more stable, showed higher Faradaic efficiency. In conclusion, diverse iron oxide nanomaterials were prepared by a simple and eco-friendly route, providing nanomaterials with high water oxidation electrocatalytic activity, which are promising catalysts based on Earth-abundant elements as an alternative to the active noble metal electrocatalysts.

Supplementary Information

Supplementary information (*Camellia sinensis* extract characterization (HPLC-DAD, qualitative tests), SEM, SEM-EDS, thermogravimetric and electrochemical data) is available free of charge at http://jbcs.sbq.org.br as PDF file.

Acknowledgments

We acknowledge Laboratório de Cristalografia e Difração de Raio-X (CBPF) for the XRD analyses, Laboratório de Catálise e Energia Sustentável (LACES/UFRJ) for thermogravimetric analyses, and Laboratório de Microscopia Eletrônica de Alta Resolução (LaMAR/CAIPE-UFF) for SEM and SEM-EDS analyses. This work was financially supported by Universidade do Estado do Rio de Janeiro (Undergraduated Scholarship PIBIC/UERJ; Programa Pró-Ciência; InovUERJ), Fundação Carlos Chagas de Amparo à Pesquisa do Estado do Rio de Janeiro-FAPERJ (CNE 2021: E-26/200.416/2023; Post-doctoral scholarship PDJ10: E-26/290.125/2020; JCNE 2023: E-26/200.201/2023; Emergentes 2019: E-26/010.002212/2019; Agrárias 2022: SEI-260003/001750/2023), Conselho Nacional de Desenvolvimento Científico e Tecnológico (PQ-2/2021: 316550/2021-3; PQ-2/2022: 306787/2022-9), and Coordenação de Aperfeiçoamento de Pessoal de Nível Superior-Brasil (CAPES) (Finance code 001).

Author Contributions

All authors contributed to the formal analysis and writing review and editing; S. L. Machado was responsible for data curation, investigation, methodology, validation, visualization, writing original draft; A. L. Silva for data curation, investigation, methodology, supervision, validation, visualization; Ana P. N. Souza for data curation, methodology; D. R. Sánchez for investigation, methodology, validation, visualization; M. Alzamora for investigation, methodology, validation, visualization; J. S. Gois for formal analysis, investigation, methodology; N. M. F. Carvalho for conceptualization, data curation, formal analysis, funding acquisition, investigation, methodology, project administration, resources, supervision, validation, visualization, writing original draft.

References

1. Kim, N.; Lee, I.; Choi, Y.; Ryu, J.; *Nanoscale* **2021**, *13*, 20374. [Crossref]
2. Zhao, M.; Li, H.; Yuan, W.; Li, C. M.; *ACS Appl. Energy Mater.* **2020**, *3*, 3966. [Crossref]
3. He, R.; Wang, C.; Feng, L.; *Chin. Chem. Lett.* **2023**, *34*, 107241. [Crossref]
4. Zhuang, Z.; Giles, S. A.; Jenness, G. R.; Abbasi, R.; Chen, X.; Wang, B.; Vlachos, D. G.; Yan, Y.; *J. Electrochem. Soc.* **2021**, *168*, 034518. [Crossref]
5. Alajmi, M. F.; Ahmed, J.; Hussain, A.; Ahamad, T.; Alhokbany, N.; Amir, S.; Ahmad, T.; Alshehri, S. M.; *Appl. Nanosci.* **2018**, *8*, 1427. [Crossref]
6. Zahra, T.; Ahmad, K. S.; Zequine, C.; Gupta, R. K.; Thomas, A. G.; Malik, M. A.; *Sustainable Energy Technol. Assess.* **2020**, *40*, 100753. [Crossref]
7. Azhar, S.; Ahmad, K. S.; Abrahams, I.; Ingsel, T.; Gupta, R. K.; El-marghany, A.; *Chem. Pap.* **2023**, *78*, 1647. [Crossref]
8. Azhar, S.; Ahmad, K. S.; Abrahams, I.; Lin, W.; Gupta, R. K.; Mazhar, M.; Ali, D.; *RSC Adv.* **2021**, *11*, 30510. [Crossref]
9. Azhar, S.; Ahmad, K. S.; Andleeb, S.; Abrahams, I.; Lin, W.; Gupta, R. K.; El-marghany, A.; *J. Appl. Electrochem.* **2024**, *54*, 963. [Crossref]
10. Silva, T. R.; Raimundo, R. A.; Silva, V. D.; Santos, J. R. D.; Araújo, A. J. M.; Oliveira, J. F. G. A.; Lima, L. C.; Silva, F. F.; Ferreira, L. S.; Macedo, D. A.; *Int. J. Hydrogen Energy* **2023**, *48*, 17160. [Crossref]
11. Chen, M.; Zhang, Z.; Zeng, C.; Jiang, J.; Gao, H.; Ai, L.; *Colloids Surf., A* **2022**, *638*, 128248. [Crossref]
12. Huang, H.; Zhao, J.; Liu, R.; *J. Colloid. Interface Sci.* **2021**, *582*, 396. [Crossref]
13. Shi, Y.; Yu, Y.; Liang, Y.; Du, Y.; Zhang, B.; *Angew. Chem., Int. Ed.* **2019**, *58*, 3769. [Crossref]
14. Carvalho, S. S. F.; Carvalho, N. M. F.; *J. Environ. Manage.* **2017**, *187*, 82. [Crossref]
15. de Souza, A. P. N.; Licea, Y. E.; Colaço, M. V.; Senra, J. D.; Carvalho, N. M. F.; *J. Environ. Chem. Eng.* **2021**, *9*, 105062. [Crossref]
16. Franco, R. T.; Silva, A. L.; Licea, Y. E.; Serna, J.; Alzamora, M.; Sánchez, D. R.; Carvalho, N. M. F.; *Inorg. Chem.* **2021**, *60*, 5734. [Crossref]

17. Perrotti, T. C.; Freitas, N. S.; Alzamora, M.; Sánchez, D. R.; Carvalho, N. M. F.; *J. Environ. Chem. Eng.* **2019**, *7*, 103237. [Crossref]
18. Nakamura, T.; Silva, F. S.; Silva, D. X.; Souza, M. W.; Moya, H. D.; *ABCS Health Sciences* **2013**, *38*, 8. [Crossref]
19. de Souza, A. P. N.; Sánchez, D. R.; Alzamora, M.; Colaço, M. V.; de Souza, M. A. V.; De Gois, J. S.; Senra, J. D.; Carvalho, N. M. F.; *Environ. Sci. Pollut. Res. Int.* **2023**, *30*, 109423. [Crossref]
20. Kilmartin, P. A.; Hsu, C. F.; *Food Chem.* **2003**, *82*, 501. [Crossref]
21. McCrory, C. C. L.; Jung, S.; Peters, J. C.; Jaramillo, T. F.; *J. Am. Chem. Soc.* **2013**, *135*, 16977. [Crossref]
22. Kumar, A.; Muhommad, J.; Purkayastha, S. K.; Guha, A. K.; Das, M. R.; Deka, S.; *ACS Sustainable Chem. Eng.* **2023**, *11*, 2541. [Crossref]
23. Kilmartin, P. A.; Zou, H.; Waterhouse, A. L.; *J. Agric. Food Chem.* **2001**, *49*, 1957. [Crossref]
24. Aliahmad, M.; Moghaddam, N. N.; *Mater. Sci.-Pol.* **2013**, *31*, 264. [Crossref]
25. Zainuri, M.; *IOP Conf. Ser.: Mater. Sci. Eng.* **2017**, *196*, 012008. [Crossref]
26. Murad, E.; *Hyperfine Interact*. **1998**, *117*, 39. [Crossref]
27. Pankhurst, Q. A.; Pollard, R. J.; *Clays Clay Miner.* **1992**, *40*, 268. [Crossref]
28. Oliveira, A. C.; Marchetti, G. S.; Carmo Rangel, M.; *J. Therm. Anal. Calorim.* **2003**, *73*, 233. [Crossref]
29. Jacob, J.; Khadar, M. A.; *J. Magn. Magn. Mater.* **2010**, *322*, 614. [Crossref]
30. Wang, F.; Qin, X. F.; Meng, Y. F.; Guo, Z. L.; Yang, L. X.; Ming, Y. F.; *Mater. Sci. Semicond. Process.* **2013**, *16*, 802. [Crossref]
31. Smith, R. D. L.; Prévot, M. S.; Fagan, R. D.; Zhang, Z.; Sedach, P. A.; Siu, M. K. J.; Trudel, S.; Berlinguette, C. P.; *Science* **2013**, *340*, 60. [Crossref]
32. Zhang, C.; Xie, Z.; Liang, Y.; Meng, D.; Wang, Z.; He, X.; Qiu, W.; Chen, M.; Liang, P.; Zhang, Z.; *Int. J. Hydrog. Energy* **2021**, *46*, 17720. [Crossref]
33. Sugawara, Y.; Kamata, K.; Hayashi, E.; Itoh, M.; Hamasaki, Y.; Yamaguchi, T.; *ChemElectroChem* **2021**, *8*, 4466. [Crossref]
34. McCrory, C. C. L.; Jung, S.; Ferrer, I. M.; Chatman, S. M.; Peters, J. C.; Jaramillo, T. F.; *J. Am. Chem. Soc.* **2015**, *137*, 4347. [Crossref]

Submitted: February 15, 2024
Published online: June 12, 2024